Optica Applicata, Vol. XLVIII, No. 4, 2018
10.5277/oa180401

Moving-aperture-based three-dimensional micro-measurement system

Shengli Fan[1, 2], Mei Yu[1*], Gangyi Jiang[1], Yigang Wang[2], Wei Wang[3], Wenda Li[3]

[1]Faculty of Information Science and Engineering, Ningbo University, Ningbo 315211, China

[2]School of Information Science and Engineering, Ningbo Institute of Technology, Zhejiang University, Ningbo 315100, China

[3]Ningbo Power Supply Company, State Grid Zhejiang Electric Power Corporation, Ningbo 315600, China

[*]Corresponding author: yumei2@126.com

To overcome the depth-of-field limitation of an optical microscope image, a three-dimensional measurement method with a superior depth-of-field is proposed. In the proposed method, light-field information of different angles is obtained by moving the aperture and the three-dimensional scene is reconstructed by using a computational reconstruction technology. First, stereo matching of different aperture position images is performed to obtain the multi-aperture imaging deviation. The focal plane moving distance is thereby estimated. Then, the relational expression between the image coordinates and the focal plane moving distance is determined according to the image coordinates. Two dimensional coordinates of the space point are obtained by the expression coefficients. Finally, the depth coordinates are computed, and three-dimensional reconstruction of the spatial points is completed. Experiments of three-dimensional measurements of the calibration board with different angles and circuit boards are conducted. The results show that the maximum error of the distance measurement is controlled into 0.84%, and the maximum angle measurement error is controlled into 4.56%.

Keywords: optical microscopy, computational photography, three-dimensional micro-measurement, moving aperture.

1. Introduction

In optical microscope imaging, the depth-of-field and lateral resolution are incompatible [1–3]. The axial dimension of the three-dimensional (3D) object to be observed under high resolution is often beyond the microscope depth-of-field. This leads to difficulties in obtaining a clear image of the whole object, and to the consequential failure of the final 3D measurement [4–6]. Therefore, techniques that increase the microscope depth-of-field while ensuring an adequate lateral resolution value to measure 3D information of the whole object comprise an intense research area in the optical microscope

field. In addition, expansion of the application range and development of measuring instruments with a superior depth-of-field have been recent subjects of interest.

In a light field camera model, light field information can be expressed using a seven dimensional plenoptic function related to 3D position (x, y, z), angle (θ, φ), frequency λ and moment t. Thus the seven dimensional plenoptic function in static monochromatic light space which frequency λ and moment t are constant can be simplified to a five-dimensional (5D) function [7]. In the classic imaging model, a two-dimensional (2D) sensor only captures 2D position (x, y) information, which leads to the loss of depth z and angle (θ, φ) information. The image blurring is caused by the diffuse circle convergence of optical signals from different angles in different space points on the imaging plane. If the optical signal of different angles can be obtained, the computational reconstruction technique can be applied to eliminate the diffuse circle and produce a clear image of the whole object. In this way, the microscope depth-of-field is increased.

In a light-field camera, light from different angles is mapped to different sensor pixels through a micro-lens array to extract the optical signal of different angles. Then, a full-focus image is obtained by computational reconstruction, and the 3D scene information is reconstructed using reconstruction parameters [7–9]. The main advantages of a light-field camera for 3D imaging are its fast capture speed and its photon efficiency, since all the photons that reach the image plane are captured. However, the lateral resolution of the image sensor in a light-field camera is sacrificed since the limited number of pixels on the sensor must be spread across position (x, y) and angle (θ, φ), which counters the objective of increasing the microscope depth-of-field for a certain lateral resolution [10]. A light source is encoded according to the position of the liquid -emitting diode (LED) array, and images of different angles are obtained. Accordingly, 3D reconstruction of the object is realized [11–13]. The method based on the LED array overcomes the limitation of sacrificing the imaging sensor lateral resolution. Nevertheless, this approach is applicable only for thin objects, which limits its application scope [13]. Both the light-field camera and LED array imaging system have some limitations on the depth-of-field expansion.

To realize 3D measurement of super depth-of-field while ensuring an adequate lateral resolution value, a 3D micro-measurement method based on a moving aperture is proposed. In the presented method, images of different angles are obtained using the moving aperture. Next, stereo matching and 3D reconstruction of the stereo vision measurement are performed to obtain a dense 3D scene graph. The micro-imaging system depth-of-field is thus expanded, it is not necessary to sacrifice the sensor lateral resolution, or measure the thin object. The proposed method can therefore be used in various applications.

2. Basic concept of proposed method

An aperture is inserted in front of the lens in the existing microscopic imaging system, such that the aperture plane is perpendicular to the optical axis. The aperture moves in the plane perpendicular to the optical axis, and different images are captured in dif-

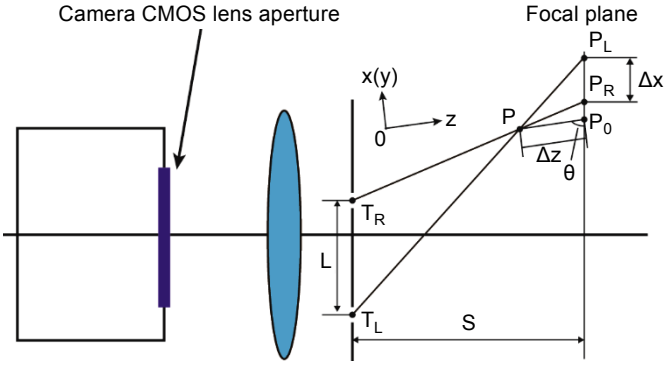

Fig. 1. Micro-imaging system structure.

ferent aperture positions. The 3D object information is obtained from these images. The aperture inserted into the system is called moving aperture.

2.1. Focal plane moving distance and multi-aperture imaging deviation

As shown in Fig. 1, for any point $P(x, y, z)$ in space, P_L and P_R are the image points corresponding to different apertures (only direction X is drawn in the figure; direction Y is similar to direction X). Assume that the center distance of the aperture corresponding to the two images is L and the distance between P_L and P_R is Δx. From the lens imaging model, the distance between the two points on the focal plane is proportional to the distance of its image points,

$$\Delta x = k\,\Delta u \tag{1}$$

where k is the scale factor, and Δx represents the distance between two points on the focal plane represented by world coordinates. In addition, Δu denotes the distance of two image points of P represented by image coordinates and is called the *multi-aperture imaging deviation*.

Point P is moved by Δz along the Z axis of the world coordinate system and results in reaching point P_0 on the focal plane. The moving distance Δz is called the *focal plane moving distance*. The angle between PP_0 and the focal plane is θ. The relationship between multi-aperture imaging deviation and focal plane moving distance can be deduced from the geometrical relation in Fig. 1 as

$$\frac{k\,\Delta u}{L} = \frac{\Delta z \sin(\theta)}{S - \Delta z \sin(\theta)} \tag{2}$$

where S is the distance between the aperture and the focal plane. In conventional microscopes, since the depth-of-field is very small, S is much larger than Δz. Therefore, the right denominator of Eq. (2) can be reduced to S:

$$\frac{k\,\Delta u}{L} = \frac{\Delta z \sin(\theta)}{S} \tag{3}$$

Alternately,

$$\Delta z = \frac{kS}{L\sin(\theta)}\Delta u \tag{4}$$

It is evident in Eq. (4) that the focal plane moving distance is proportional to the multi-aperture imaging deviation in the conventional microscope. For the 3D microscopic measurement system based on a moving aperture, the aperture is inserted at the front end of the lens to expand the depth-of-field of the imaging system. Thus, the condition that S is far greater than Δz is invalid. Moreover, there exists a non-linear relationship between focal plane moving distance Δz and multi-aperture imaging deviation Δu.

2.2. Spatial coordinates estimation

Point $P(x, y, z)$ in space is moved along the Z axis of the world coordinate system, *i.e.*, only the value of z is changed and the value of x and y are unchanged. The image coordinates of point P corresponding to aperture T_{L} will change. The relationship between the moving distance and image coordinates can be expressed as:

$$\begin{cases} u = f_{(x,\,y)}(\Delta z) \\ v = g_{(x,\,y)}(\Delta z) \end{cases} \tag{5}$$

where (u, v) are the image coordinates and $f_{(x,\,y)}$, $g_{(x,\,y)}$ are the function representing the relationship. The function arguments relate to (x, y).

It is experimentally determined that $f_{(x,\,y)}$ and $g_{(x,\,y)}$ are quadratically correlated:

$$\begin{cases} u = a_f \Delta z^2 + b_f \Delta z + d_f \\ v = a_g \Delta z^2 + b_g \Delta z + d_g \end{cases} \tag{6}$$

The relationship between the coefficients of the two functions is described as:

$$\begin{bmatrix} a_f \\ d_f \\ a_g \\ d_g \end{bmatrix} = T \begin{bmatrix} b_f \\ b_g \\ 1 \end{bmatrix} \tag{7}$$

where the coefficient relation matrix

$$T = \begin{bmatrix} k_{a,f} & 0 & c_{a,f} \\ k_{d,f} & 0 & c_{d,f} \\ 0 & k_{a,\,g} & c_{a,\,g} \\ 0 & k_{d,\,g} & c_{d,\,g} \end{bmatrix} \tag{8}$$

Substituting Eq. (7) into Eq. (6), we obtain

$$\begin{cases} b_{\mathrm{f}} = \dfrac{u - c_{a,f}\Delta z^2 - c_{d,f}}{k_{a,f}\Delta z^2 + \Delta z + k_{d,f}} \\ b_{\mathrm{g}} = \dfrac{v - c_{a,g}\Delta z^2 - c_{d,g}}{k_{a,g}\Delta z^2 + \Delta z + k_{d,g}} \end{cases} \tag{9}$$

Thus, the function coefficient (b_f, b_g) can be determined by (u, v) and Δz. The relationship between (b_f, b_g) and (x, y) is given by

$$M\begin{bmatrix} x \\ y \\ 1 \end{bmatrix} = \begin{bmatrix} b_f \\ b_g \\ 1 \end{bmatrix} \tag{10}$$

where M is the coefficient coordinate matrix. The coordinates (x, y) of the space points can be obtained from Eq. (10).

Assuming that P is moved by Δz_0 along the Z axis of the world coordinate system to reach the focal plane, we obtain

$$z = \Delta z_0 - \Delta z \tag{11}$$

3. Three-dimensional micro-measurement method

The proposed 3D micro-measurement method realizes the 3D reconstruction of a microscopic scene as shown in Fig. 2. This method is divided into two parts: system calibration and 3D measurement.

In the system calibration, several sets of calibration images of a calibration board corresponding to different positions are captured by the moving aperture. Feature matching is applied to image pairs with different apertures at the same position. Several standard matching pairs are obtained by combining their mutual positional relations. According to the relationship between the focal plane moving distance Δz and multi-aperture imaging deviation Δu, the relation equation and its coefficients are obtained. The relation curves between the image coordinate and focal plane moving distance Δz are fitted, and T in Eq. (7) is calibrated. Moreover, matrix M in Eq. (10) can be calibrated using (b_f, b_g) and (x, y). The z values of the focal imaging points are obtained from the relationship between z values of the point and multi-aperture imaging deviation Δu. The spatial equation of the focal plane can be obtained by plane fitting.

In the 3D measurement, the moving aperture is used to image the object, and a pair of images is obtained. Stereo matching is used to obtain a certain number of matching pairs that can be expressed by using a disparity map. For each matching pair, multi-aperture imaging deviation is calculated, and the corresponding focal plane moving distance is estimated. By substituting the values of (u, v) and Δz in Eq. (9), the coefficients

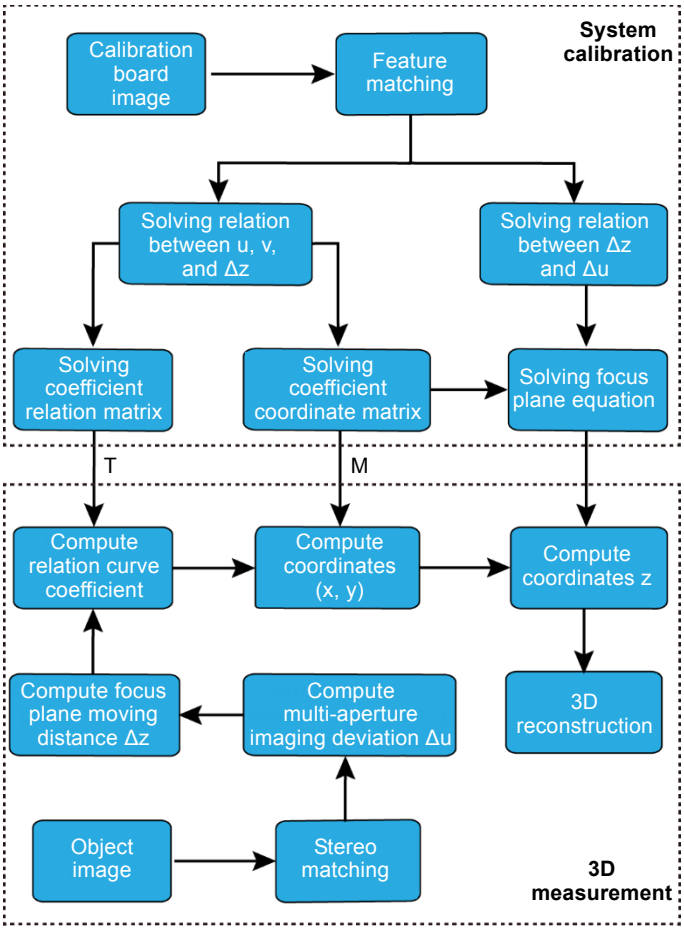

Fig. 2. Framework of the proposed 3D micro-measurement method based on a moving aperture.

are determined. Using Eq. (10), the (x, y) coordinates of the space point are calculated. The z coordinate is obtained by Eq. (11) and the 3D reconstruction of one point is completed. The 3D reconstruction of the whole object can be achieved by repeating the above process.

4. Results and discussion

4.1. Experimental setup

The experimental setup is shown in Fig. 3. All objects were imaged using a Canon EOS700D digital single-lens reflex (SLR) camera and a Canon MP-E 65 mm $f/2.8$ 1–5× macro lens. The diameter of the aperture was 2 mm; the moving distance was 6 mm.

A board printed with solid dots was placed on a one-dimensional motorized stage (Chuo Seiki XA07A-R2H, 2 μm/step) to be moved along the Z axis. The diameter of

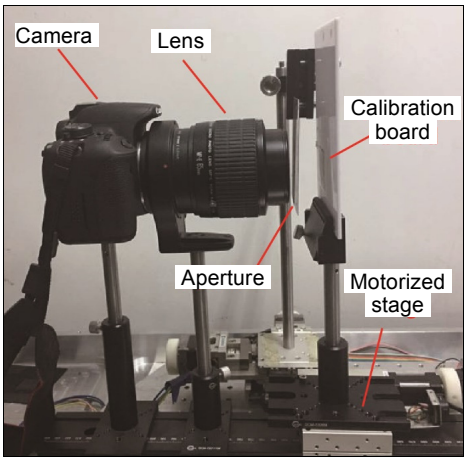

Fig. 3. Experimental setup of 3D micro-measurement system based on a moving aperture.

the solid dots in a 21 × 21 array was 0.5 mm and the pitch was 1 mm. The motorized stage was controlled to move 15.9 mm with equal steps of 0.1 mm to divide the calibration board into 160 equally spaced positions. In each position, a pair of images corresponding to different apertures was captured. Thus, 320 images were obtained. As

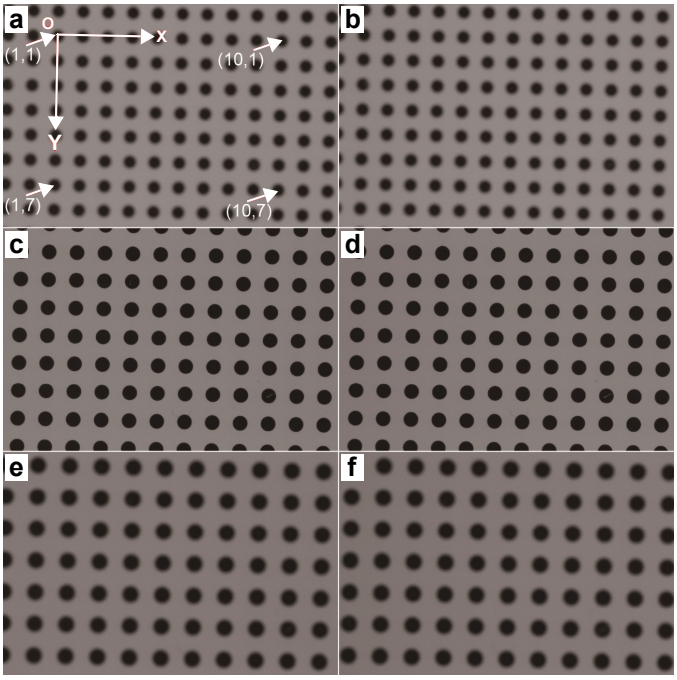

Fig. 4. Calibration board image: first pair of images (**a**, **b**), 80th pair of images (**c**, **d**), and 160th pair of images (**e**, **f**).

shown in Fig. 4, the first, 80th and 160th pairs of images are listed. By taking the center of a solid dot on the board as the coordinate origin, the world coordinate system was established. Accordingly, the point in the center of the solid dots of the same row was considered the *X* axis, and the point in the center of solid dots of the same column was the *Y* axis. The moving direction of the motorized stage was the *Z* axis, as shown in Fig. 4**a**.

4.2. Dot center extraction

First, the captured 320 images were pretreated by graying and binarization to obtain the proper binary images. Then, the solid dot regions were segmented by a region growing algorithm, and the coordinates of the region geometric center were calculated. At the same time, the matching pairs were obtained by the positional relation between the solid dots for two images of different apertures in the same position. Overall, 70 matching pairs were extracted and arranged in seven rows and ten columns, with (1, 1) representing the upper left corner and (10, 7) representing the lower-right corner, as shown in Fig. 4**a**.

4.3. Depth-of-field

As mentioned above, the aperture of the imaging system was greatly reduced and the depth-of-field was expanded. As shown in Figs. 5**a** and 5**c**, in a certain position, the system both with and without the aperture produces clear images. When the calibration board is moved by 2.5 mm along the *Z* axis, the images captured by the system without the aperture become blurred, whereas the images captured by the proposed system with the aperture remain clear, as shown in Figs. 5**b** and 5**d**.

The focal characteristics curve of the sharpness values of the calibration board image in every position and coordinate *z* is shown in Fig. 6. The sharpness values of images

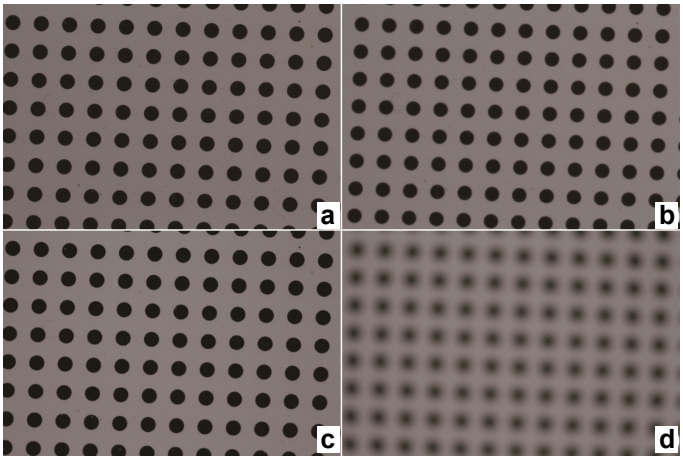

Fig. 5. Depth-of-field range analysis. Image captured by the proposed system in the focal position (**a**), the proposed system at 2.5 mm from the focal position (**b**), the system without the aperture in the focal position (**c**), and the system without the aperture at 2.5 mm from the focal position (**d**).

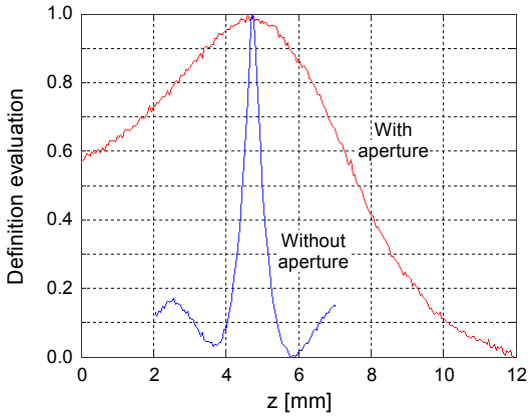

Fig. 6. Focal characteristics curve.

are represented using the Tenengrad function. Compared to the system without the aperture, the clear imaging range of the proposed system is much greater.

4.4. Relationship between focal plane moving distance and multi-aperture imaging deviation

When the multi-aperture imaging deviation of a point in space was zero, the point was located on the focal plane. The multi-aperture imaging deviation of different points on the calibration board became zero in different z positions. At this moment, the point was on the focal plane. The center of the solid dots on the calibration board was taken as the reference point, and 7 × 10 points on the focal plane were obtained. The focal plane could be obtained by plane fitting, as shown in Fig. 7, where the focal plane and calibration board plane are at a certain angle.

Assuming that the relationship between the focal plane moving distance and multi -aperture imaging deviation was linear, a blue line was drawn, as shown in Fig. 7**b**. It

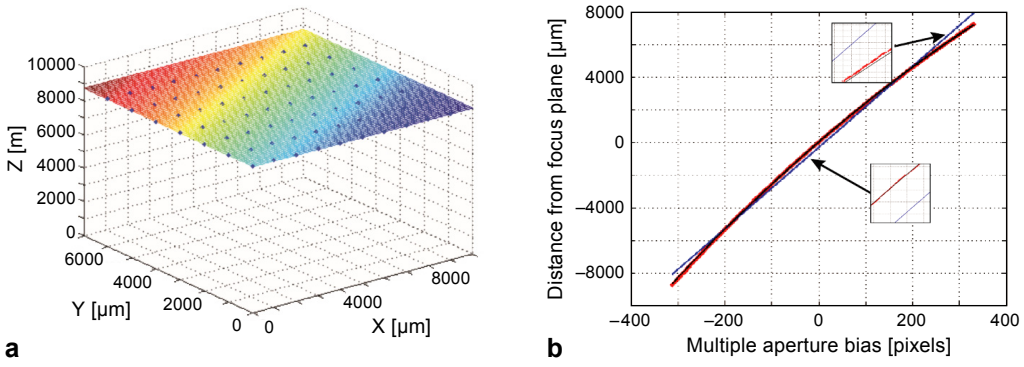

Fig. 7. Focal plane fitting (**a**). Relation of focal plane moving distance Δz and multi-aperture imaging deviation Δu (**b**).

is observed in the figure that a large fitting error occurs. The aperture diameter is too small to markedly expand the depth-of-field of the imaging system, which invalidates the condition that S is much larger than z. A nonlinear relationship exists between z and multi-aperture imaging deviation. The two polynomials are used to fit the curve, which greatly reduces the fitting error, as shown by the black line in Fig. 7**b**.

The focal plane moving distance of the space point could be obtained by the multi -aperture imaging deviation. The z coordinate of the corresponding focal point could be obtained by the (x, y) coordinates of the space point; then, the z coordinates of the space point were obtained.

4.5. Image coordinate and focal plane moving distance

From Eq. (6), it is known that the image coordinates vary with focal plane moving distance, and the change relation can be expressed by a quadratic polynomial. For each solid dot on the calibration board, the relation curve is drawn by extracting the central coordinates of each Z position corresponding to the image and curve fitting (Fig. 8). Four curves of the center of the solid dots at different positions are drawn in Fig. 8.

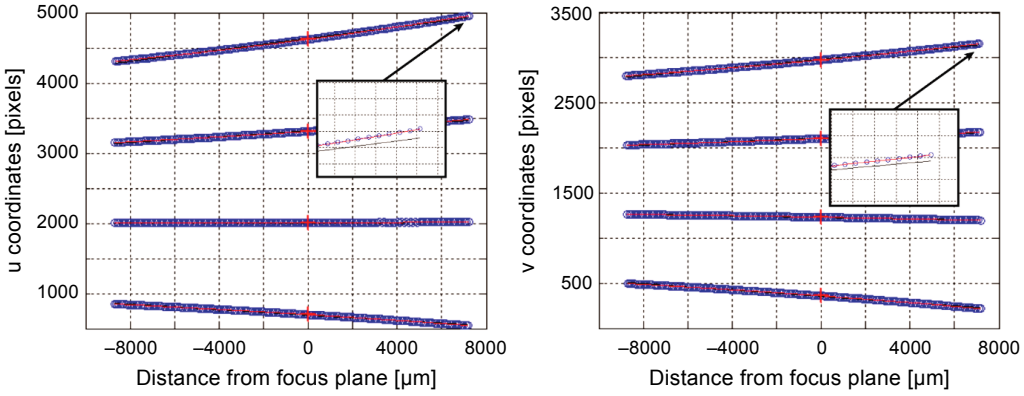

Fig. 8. Relationship between the image coordinates and focal plane moving distance: u *vs.* Δz (**a**) and v *vs.* Δz (**b**).

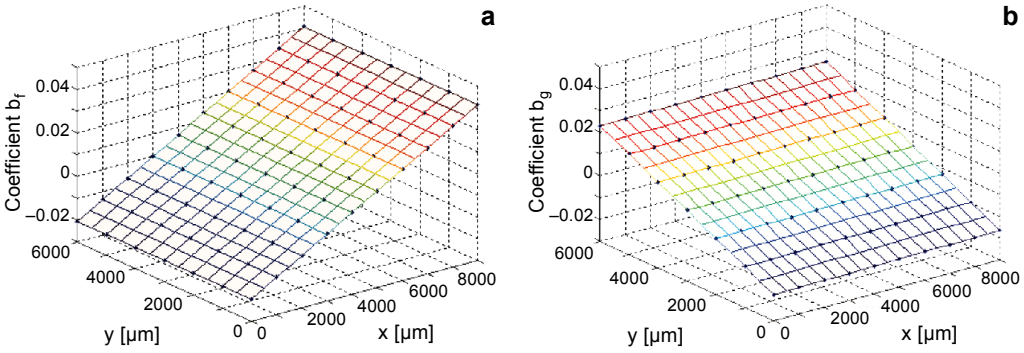

Fig. 9. Curve coefficients and the spatial coordinates (x, y). Coefficient b_f *vs.* (x, y) (**a**) and b_g *vs.* (x, y) (**b**).

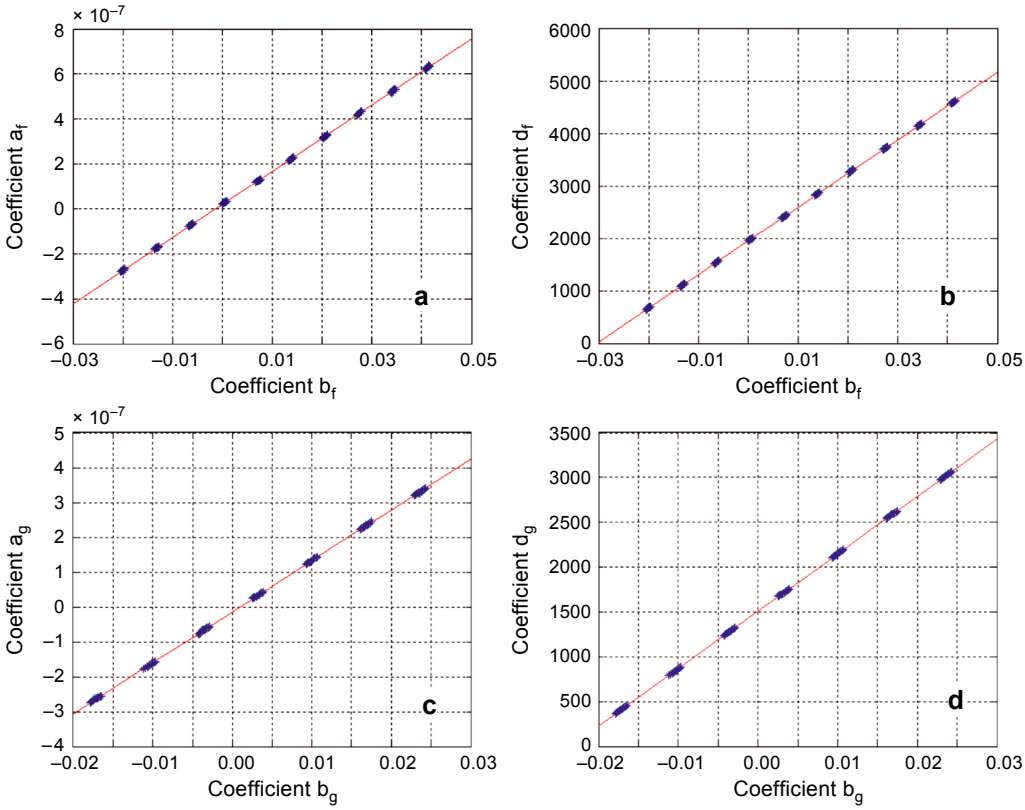

Fig. 10. Relationships between coefficients: a_f *vs.* b_f (**a**), d_f *vs.* b_f (**b**), a_g *vs.* b_g (**c**), and d_g *vs.* b_g (**d**).

The black line is the result of linear fitting; the red line is the result of quadratic polynomial fitting. It is observed that a quadratic polynomial relationship exists between the image coordinates and Δz. The coefficients of the quadratic polynomial corresponding to different solid dots are different.

Each solid dot corresponds to a curve, *i.e.*, the coefficients are determined by the spatial coordinates (x, y). By point plotting and plane fitting, the relationship between coefficient b and the spatial coordinates (x, y) is obtained as shown in Fig. 9.

From Eq. (7), it is evident that the relationships between a, d, and b are linear, and the coefficients can be obtained by linear fitting as shown in Fig. 10. The results of the above calibration process are shown in Table 1.

4.6. Calibration results evaluation

The calibration board was driven by a precision angular rotation table to rotate at a specific angle. The calibration results were evaluated by the center distance of the solid dots and the angle between the boards at different positions. In the experiment, the standard distance between the centers of the solid dots was 1 mm. The board rotates

T a b l e 1. Parameter calibration results.

Focal plane equation	$z = 8.6943 \times 10^3 - 0.0041x + 0.0104y$
Relationship of focal plane moving distance Δz and multi-aperture imaging deviation Δu	$\Delta z = -0.0027 + 24.8756\Delta u - 0.0096\Delta u^2$
Relationship of (b_f, b_g) and (x, y)	$\begin{bmatrix} b_f \\ b_g \\ 1 \end{bmatrix} = \begin{bmatrix} 6.7977 \times 10^{-6} & -1.6149 \times 10^{-7} & -0.0196 \\ 1.5935 \times 10^{-7} & 6.7953 \times 10^{-6} & -0.0179 \\ 0 & 0 & 1 \end{bmatrix} \begin{bmatrix} x \\ y \\ 1 \end{bmatrix}$
Relationship of coefficients	$\begin{cases} a_f = 1.4731 \times 10^{-5} b_f + 2.0620 \times 10^{-8} \\ d_f = 6.4068 \times 10^4 b_f + 1.9548 \times 10^3 \\ a_g = 1.4615 \times 10^{-5} b_g - 1.3818 \times 10^{-8} \\ d_g = 6.4117 \times 10^4 b_g + 1.5078 \times 10^3 \end{cases}$

T a b l e 2. Calibration result evaluation.

Plane	Direction	RMSE [μm]	Min [μm]	Max [μm]	Avg [μm]
Π_1	Horizontal	4.8286	–1.2676	8.4174	3.4442
	Vertical	2.8651	1.3631	4.7902	–1.6746
Π_2	Horizontal	3.6221	–6.2525	3.0489	1.2672
	Vertical	1.5471	–2.6293	–0.3150	0.5673
Π_3	Horizontal	3.5908	–3.3981	6.7564	2.7805
	Vertical	1.7636	0.5840	3.0187	–1.4553
Π_4	Horizontal	3.3797	–4.4176	5.7370	1.6924
	Vertical	0.8453	–1.2843	2.0718	0.3129
		Π_1 and Π_2	Π_2 and Π_3	Π_3 and Π_4	
Included angle [deg]		6.1225	5.8180	5.7262	
Error [%]		2.04	3.03	4.56	

four times at 6° each time. The root mean square error (RMSE) was used to evaluate the accuracy of the 3D measurement [14, 15]

$$\mathrm{RMSE} = \sqrt{\frac{\sum_{i=1}^{n} (d_i - d_s)^2}{n}} \tag{12}$$

where d_i is the measured center distance of the solid dots and d_s is the standard distance which is 1 mm in the experiment; n is the number of the distance measured. The results are shown in Table 2. The distances include two directions: horizontal and vertical.

As shown in Fig. 11, the center of the solid dots at different positions is drawn and four space planes are obtained by plane fitting. The angles between the adjacent planes are 6.1225°, 5.8180°, and 5.7262°, with a maximum error of 4.56%.

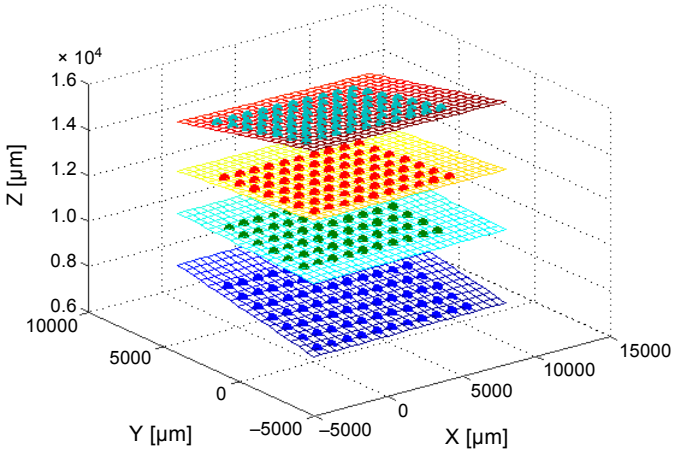

Fig. 11. Three-dimensional reconstruction of the calibration plate at different angles.

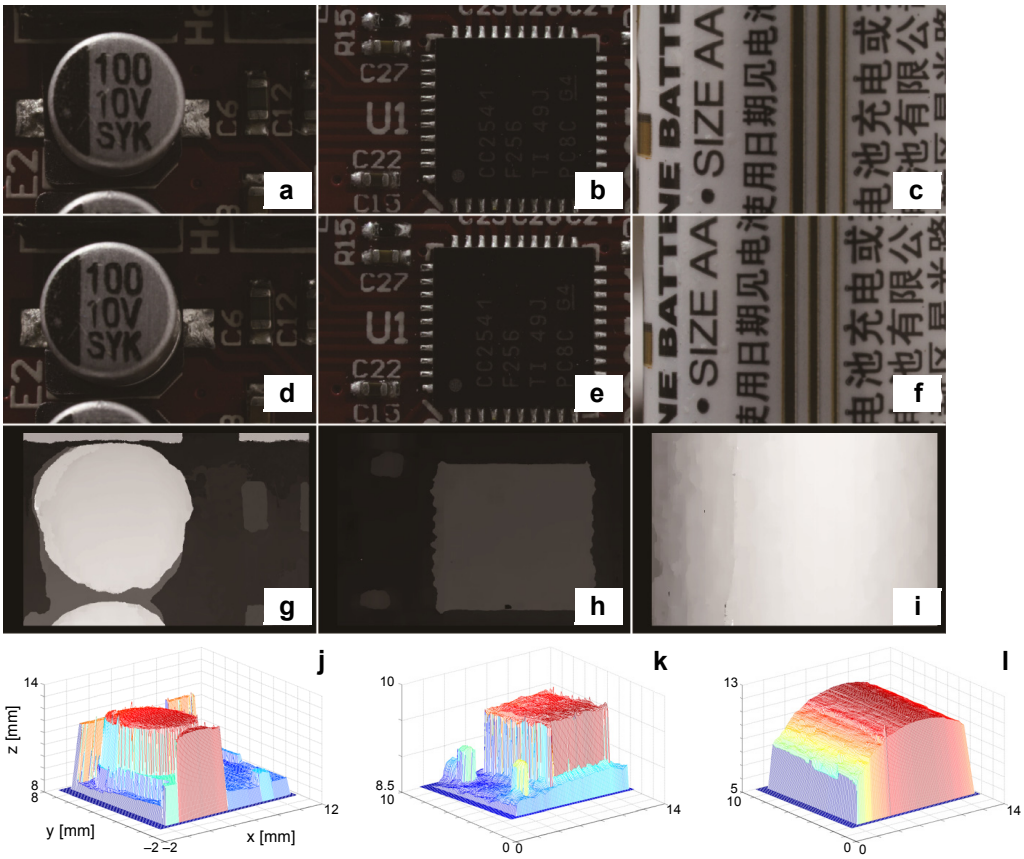

Fig. 12. Three-dimensional reconstruction of test samples: images corresponding to one aperture (**a**, **b**, **c**), images corresponding to another aperture (**d**, **e**, **f**), stereo matching disparity maps (**g**, **h**, **i**), and reconstruction of 3D model (**j**, **k**, **l**).

4.7. Three dimensional reconstruction of actual objects

An electrolytic capacitor, a chip and a battery are chosen as test samples. Two images of each sample were obtained by moving the aperture, as shown in Figs. 12**a**–12**f**. Disparity maps are obtained using a stereo matching algorithm, as shown in Figs. 12**g**–12**i**. The coordinates of the right and left matching points were obtained using the disparity maps. The 3D coordinates of the spatial points were obtained by the proposed 3D measurement method. The 3D model is shown in Figs. 12**j**–12**l**.

5. Conclusion

In this paper, a 3D measurement method based on a moving aperture was proposed. Different images were obtained by changing the aperture position, and a stereo vision method was used to reconstruct the 3D scene. In the proposed approach, the aperture enlarges the depth-of-field of the measurement system, such that the original linear model is not applicable. By analyzing the principle of super depth-of-field micro-imaging, a 3D measurement method based on a nonlinear model was established. The model parameters were calibrated using a calibration board and precise motorized stages. Experimental results showed that the maximum error of distance measurement was 0.84%, and the maximum angle measurement error was 4.56%.

Acknowledgements – This work was supported by the Natural Science Foundation of China under Grant No. 61671258, the National High-tech R&D Program of China under Grant No. 2015AA015901, and the Natural Science Foundation of Zhejiang Province under Grant No. LY15F010005. It was also sponsored by the K.C. Wong Magna Fund of Ningbo University.

Reference

[1] EN BO, LINBO LIU, *Spectral domain optical coherence tomography with extended depth-of-focus by aperture synthesis*, Proceedings of SPIE 10024, 2016, article ID 1002451.

[2] YAWEI WANG, LI ZHANG, YING JI, YUANYUAN XU, MIN BU, YINGZHOU CHEN, *3D morphological reconstruction of the red blood cell based on two phase images*, Optica Applicata 45(2), 2015, pp. 173–182.

[3] XIAOQING XU, YAWEI WANG, YUANYUAN XU, WEIFENG JIN, *Simultaneous measurement of refractive index and thickness for optically transparent object with a dual-wavelength quantitative technique*, Optica Applicata 46(4), 2016, pp. 597–605.

[4] AMBIKUMAR A.S., BAILEY D.G., SEN GUPTA G., *Extending the depth of field in microscopy: a review*, Proceedings of the 2016 International Conference on Image and Vision Computing New Zealand. November 21–22, 2016, Palmerston North, New Zealand, IEEE, pp. 185–190.

[5] KI-CHUL KWON, ERDENEBAT M.-U., ALAM M.A., YOUNG-TAE LIM, KWANG GI KIM, NAM KIM, *Integral imaging microscopy with enhanced depth-of-field using a spatial multiplexing*, Optics Express 24(3), 2016, pp. 2072–2083.

[6] SHAIN W.J., VICKERS N.A., GOLDBERG B.B., BIFANO T., MERTZ J., *Extended depth-of-field microscopy with a high-speed deformable mirror*, Optics Letters 42(5), 2017, pp. 995–998.

[7] PÉGARD N.C., HSIOU-YUAN LIU, ANTIPA N., GERLOCK M., ADESNIK H., WALLER L., *Compressive light-field microscopy for 3D neural activity recording*, Optica 3(5), 2016, pp. 517–524.

[8] LEVOY M., REN NG, ADAMS A., FOOTER M., HOROWITZ M., *Light field microscopy*, ACM Transactions on Graphics 25(3), 2006, pp. 924–934.

[9] JONGHYUN KIM, YOUNGMO JEONG, HYUNGJIN KIM, CHANG-KUN LEE, BYEONGMOON LEE, JISOO HONG, YOUNGMIN KIM, YONGTAEK HONG, SIN-DOO LEE, BYOUNGHO LEE, *F-number matching method in light field microscopy using an elastic micro lens array*, Optics Letters 41(12), 2016, pp. 2751–2754.

[10] KALANTARI N.K., WANG T.-C., RAMAMOORTHI R., *Learning-based view synthesis for light field cameras*, ACM Transactions on Graphics 35(6), 2016, article ID 193.

[11] WETZSTEIN G., HEIDRICH W., RASKAR R., *Computational Schlieren photography with light field probes*, International Journal of Computer Vision 110(2), 2014, pp. 113–127.

[12] TIAN L., WALLER L., *Quantitative differential phase contrast imaging in an LED array microscope*, Optics Express 23(9), 2015, pp. 11394–11403.

[13] GUOAN ZHENG, HORSTMEYER R., CHANGHUEI YANG, *Wide-field, high-resolution Fourier ptychographic microscopy*, Nature Photonics 7(9), 2013, pp. 739–745.

[14] DUSSELDORP J.K., STAMATAKIS H.C., REN Y., *Soft tissue coverage on the segmentation accuracy of the 3D surface-rendered model from cone-beam CT*, Clinical Oral Investigations 21(3), 2017, pp. 921–930.

[15] WEISS M., BARET F., *Using 3D point clouds derived from UAV RGB imagery to describe vineyard 3D macro-structure*, Remote Sensing 9(2), 2017, p. 111.

Received August 15, 2017
in revised form February 10, 2018